Self-Assembly of α-Functionalized Terthiophenes on Gold

B. Liedberg,* Z. Yang, and I. Engquist

Laboratory of Applied Physics, Linköping University, S-58183 Linköping, Sweden

M. Wirde and U. Gelius

Physics Department, University of Uppsala, S-75121 Uppsala, Sweden

G. Götz and P. Bäuerle

Institue of Organic Chemistry II, University of Ulm, Albert-Einstein-Allee 11, D-89081 Ulm, Germany

R.-M. Rummel, Ch. Ziegler, and W. Göpel

Institute of Physical and Theoretical Chemistry, University of Tübingen, Auf der Morgenstelle 8, D-72076, Germany

Received: January 16, 1997[⊗]

α-Functionalized terthiophenes containing disulfide ($-S-T_3-H)_2$ and alkanethiol ($HS-(CH_2)_{11}-T_3-H$) anchoring groups have been synthesized for direct immobilization onto gold. Monolayer structures of these compounds are prepared by spontaneous assembly from ethanol solutions on evaporated gold substrates and thoroughly characterized by ellipsometry, contact angle goniometry, infrared and X-ray photoelectron spectroscopy, and cyclic voltammetry. The two molecules coordinate to the gold substrate exclusively via the anchoring groups upon formation of gold−thiolate bonds. The kinetics of monolayer formation vary dramatically for the two compounds. The alkanethiol analogue assembles rapidly, within a few minutes, and forms a densely packed and highly organized monolayer, with the alkyl chains in an almost perfect all-trans conformation and the $C_\alpha-C_\alpha$ axis of the α-T_3 units tilted about 14° away from the surface normal. The assembly process is much slower for the disulfide, but an organized monolayer with an average α-T_3 chain tilt of about 33° will eventually form when the assembly is allowed to equilibrate with a solution containing the disulfide for at least 1 day. Moreover, the two monolayer assemblies also display a remarkably different electrochemical behavior. The heterogeneous electron-transfer rate at the disulfide-covered gold substrate is almost indistinguishable from that at bare gold, suggesting that the assembly contains a large number of easily accessible defects. An alternative mechanism for explaining the large electron-transfer rate involving electronic coupling via the conjugated π-system of the α-T_3 units is also proposed. The electrochemical response is significantly reduced for the $HS-(CH_2)_{11}-T_3-H$ assembly, but another type of defects, the so-called "shallow defects" originating from sparsely populated areas on the electrode surface, can be identified.

Introduction

Polymeric materials with conjugated π-electron systems have attracted considerable interest during recent years because of their promising electronic properties. The polythiophenes are perhaps the most thoroughly investigated and well-characterized system.[1,2] These one-dimensional conductors are potentially important candidates for a broad range of applications in the ever-growing field of molecular electronics including, for example, molecular wires and switches.[3,4] Serious drawbacks of the polythiophenes are, however, their low solubility and processability in common organic solvents. These limitations have been tackled by introducing alkyl, aryl, and even more sophisticated functions at the β-position(s) prior to polymerization. Simple spin-casting techniques recently have been employed with great success to fabricate, e.g., voltage-controlled multiple-color LEDs from polymer blends based on such materials.[5] The polythiophenes also have been functionalized with molecular recognition centers as crown ethers[6] and glucose oxidase[7] for sensor applications, as well as with acceptor−donor functions[8] for information storage. An alternative approach which, at least in part, solves the problem with low solubility and processability of the polythiophenes is to use oligothiophenes $H-T_n-H$ ($2 < n < 12$) or "end-capped" analogues as building block for the development of novel materials.[9] The stepwise synthesis of these compounds offers large freedom in terms of designing materials with well-defined conjugation lengths and substitution patterns.[9,10] The oligothiophenes also have found applications as components in electronic devices, for example, as light emitting diodes[11,12] and field-effect transistors,[13,14] and the properties of these devices seem comparable to those prepared from their long-chain analogues, the polythiophenes.

Attachment and organization of the oligothiophenes into functional supramolecular assemblies on solid surfaces is a problem of its own which must be solved before interfacing them with conventional electronic devices. Spin-casting techniques are, as mentioned above, often used to prepare thin films of soluble oligomers. However, these films normally suffer from low molecular organization(orientation). Horowitz and co-workers[15] recently presented a promising method for the preparation of single crystals of unsubstituted sexithiophene (T_6). Plates a few tens of a micrometer thick and some millimeters

* Corresponding author. Phone +46-13-281877. Fax: +46-13-288969. E-mail: bol@ifm.liu.se. Visiting scientist at the University of Tübingen, Germany (1995−1997).

⊗ Abstract published in *Advance ACS Abstracts,* July 1, 1997.

S1089-5647(97)00229-0 CCC: $14.00

SCHEME 1

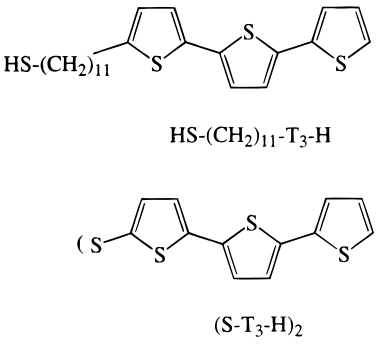

long could be prepared by a vacuum sublimation technique. We have adopted a different approach by combining the oligothiophenes with the well-established organosulfur surface chemistry[16−19] for spontaneous solution assembly onto gold substrates. Although gold is normally not considered to be a suitable material in conventional electronics, it is becoming increasingly important as substrate material in optical,[20] electrochemical,[21] and surface and bulk acoustic[22] sensing devices. Thus, the main objective with this study is to develop novel sensing interfaces "templates" based on functionalized oligothiophenes. Two α-functionalized terthiophenes with alkanethiol and disulfide anchoring groups were synthesized for that purpose (Scheme 1).

This is the first paper in a series describing the physical characterization of these monolayer assemblies. Ellipsometry and contact angle measurements are used to extract information about the kinetics of monolayer formation, infrared and X-ray photoelectron spectroscopy for obtaining structural data, and finally cyclic voltammetry for addressing the redox behavior of the assemblies and their defect structure. This is to our knowledge the first complete analysis of the self-assembly properties of alkythiol and disulfide-derivatized terthiophenes on gold. However, similar molecules have analyzed before on platinum and gold, though with a limited number of experimental techniques.[23]

Experimental Section

Materials and Sample Preparation. *Substrate preparation:* The gold substrates were prepared in a Balzers UMS 500 P electron beam evaporation system operating at a base pressure $<2-10^{-9}$ Torr. Gold 99.99% (Ädelmetall, Malmö) was evaporated to a thickness of about 2000 Å, using an evaporation rate of 5 Å/s, onto precut silicon (100) substrates which were precoated with 30 Å thick adhesion layer of titanium (Balzers 99.9%). Gold substrates prepared in this way have been characterized before with X-ray diffraction (XRD), transmission electron microscopy (TEM), and scanning tunneling microscopy (STM) and found to have a grains 200−500 Å with large flat (111) terraces.[24] A cleaning procedure (TL1) in a mixture of five parts of MilliQ water, one part of ammonia (25%), and one part of hydrogen peroxide (30%) at 80 °C for 5 min was employed to remove organic contaminants before the substrates were immersed in the sample solutions. Recent AFM studies have also shown that the grain size increases to 500−1000 Å and that the roughness decreases (≈50%) upon TL1 cleaning.

Chemicals: The synthesis of the compounds used in this paper is shortly given. Bis-(2,2′:5′,2″-terthien-5-yl)disulfide $(-S-T3-H)_2$ was obtained by lithiation of α-terthiophene with *n*-butyllithium and successive reaction of the monolithiated species with elemental sulfur. After chromatographic workup of the intermediate corresponding thiol the disulfide is obtained in analytically pure form (58% yield). Analytical data: mp 172−173 °C. IR (KBr, cm^{-1}) 3078, 3066 (m); 1494, 1455, 1426, 1418 (m); 865, 837 (m); 793, 703, 690 (s). ^{1}H NMR ($CDCl_3$) δ 7.363 (d, $^3J = 3.6$ Hz; 1H; H4), 7.248 (dd, $^3J = 5.1$ Hz, $^4J = 1.1$ Hz; 1H; H5″), 7.200 (dd, $^3J = 3.6$ Hz; $^4J = 1.2$ Hz; 1H; H3″), 7.129 (d, $^3J = 3.8$ Hz; 1H; H3′), 7.100 (d, $^3J = 3.8$ Hz; 1H; H3), 7.064 (d, $^3J = 3.8$ Hz; 1H; H4′), 7.037 (dd, $^3J = 3.6$ Hz; $^3J = 5.1$ Hz; 1H; H4″). ^{13}C NMR ($CDCl_3$) δ 143.9 (C^q, C5); 137.4 (C^q); 136.9 (C^t, C4); 136.8 (C^q); 135.3 (C^q); 134.4 (C^q); 128.0 (C^t); 125.3 (C^t); 124.9 (C^t); 124.4 (C^t); 124.1 (C^t); 123.9 (C^t). MS [FD; 8 kV; 323 K] *m*/*z* 558 [M^+, 100%], 279 [$M/2^+$, 8.03%]. Anal. Calcd for $C_{24}H_{14}S_8$ (558.90): C, 51.58; H, 2.52; S, 45.90. Found: C 51.73; H 2.55; S 45.96.

11-(2,2′:5′,2″-terthien-5-yl)undec-1-ylthiol $(HS-(CH_2)_{11}-T_3-H)$ was prepared in a seven-step synthesis starting from α-bithiophene. Friedel−Crafts acylation of the latter with 11-bromoundecanoic acid chloride and $SnCl_4$ yields the acylated bithiophene (78% yield) which is converted with hydrochinonmonomethyl ether to the corresponding diether (83% yield). Wolff−Kishner reduction of the keto group (93% yield) and succesive cleavage of the ether group with BBr_3 yields 5-(11-bromoundecyl)-2,2′-bithiophene (62% yield). Selective bromination of the latter with the system NBS/DMF (87% yield) and successive nickel-catalyzed cross-coupling with 2-thienylmagnesium bromide results in the corresponding 5-(11-bromoundecyl)-2,2′:5′,2″-terthiophene (85% yield). Final transformation to the thiol was performed with thiourea to yield pure 11-(2,2′:5′,2″-terthien-5-yl)undec-1-ylthiol $(HS-(CH_2)_{11}-T_3-H)$ in 85% yield. Analytical data: mp 83−84 °C. IR (KBr, cm^{-1}) 3097, 3072 (m); 2923, 2847 (s); 1512, 1466, 1454, 1428 (m/s); 836(m); 792, 711 (s). ^{1}H NMR ($CDCl_3$) δ 7.190 (dd, $^3J = 5.1$ Hz; $^4J = 1$ Hz; 1H; H5″), 7.144 (dd, $^3J = 3.5$ Hz, $^4J = 1$ Hz; 1H; H3″), 7.044 (d, $^3J = 3.7$ Hz; 1H; H4′), 7.003 (dd, $^3J = 3.7$ Hz; $^3J = 5$ Hz; 1H; H4″), 6.981 (d, $^3J = 3.4$ Hz; 1H; H3′), 6.968 (d, $^3J = 3.1$ Hz; 1H; H4), 6.669 (d, $^3J = 3.6$ Hz; 1H; H3), 2.779 (t, $^3J = 7.5$ Hz; 2H; $-CH_2-T_3$), 2.509 (dt, $^3J = 7.4$ Hz; 2H; $-CH_2-S-$), 1.698−1.567 (m; 4H; $-CH_2-[CH_2T_3]/-CH_2-[CH_2S]$), 1.319 (t, $^3J = 7.7$ Hz; 1H; −SH), 1.30−1.20 (m; 14H; $-CH_2-$). ^{13}C NMR ($CDCl_3$) δ 145.65 [C5, C^q], 137.36 [C^q], 136.88 [C^q], 135.64 [C^q], 134.54 [C^q], 127.91 [C^t], 124.90 [C^t], 124.33 [2 × C^t], 123.56 [2 × C^t], 123.43 [C^t], 34.14 (C^k), 31.66 (C^a), 30.26 (C^b), 29.58 (C^e, C^f, C^g), 29.42 (C^d), 29.15 (C^h, C^c), 28.47 (C^i), 24.75 (C^l). MS [EI; 70 eV] *m*/*z* 434 [M^+,100%], 261 [$M^+ - ((CH_2)_{10}-SH)$, 49.41%]. Anal. Calcd for $C_{23}H_{30}S_4$ (434.76): C, 63.54; H, 6.96; S, 29.50. Found: C 63.63; H 6.93; S 29.34.

A reference disulfide $(-S-(CH_2)_{16}-OH)_2$ was obtained from Biacore AB, Uppsala, Sweden, as a generous gift from Drs. S. Löfås and B. Johnsson.

Monolayer preparation: The adsorption experiments were performed in closed polypropylene containers at a concentration of 1 mM in EtOH 99.5% (Kemetyl, Stockholm) for 48 h unless otherwise stated in the text. After 48 h the samples were rinsed in EtOH followed by ultrasonication for 5 min in EtOH and final drying in N_2.

Analytical Techniques. *Ellipsometry:* The ellipsometric measurements were performed with an automatic Rudolph Research AutoEl III ellipsometer equipped with a He−Ne laser ($\lambda = 632.8$ nm). The angle of incidence was 70° with respect to the surface normal. The ellipometric readings Δ and Ψ were recorded as a function of immersion time of the gold substrate in the sample solution in order to obtain information about the kinetics of monolayer formation. No attempts, however, were made to fit the Δ and Ψ values to an optical model of the monolayers because of the absence of reliable anisotropic optical constants for the α-T_3 unit in the literature.

Contact angle measurements: The advancing and receding contact angles with deionized and purified MilliQ water (>18 MΩ cm) were measured in laboratory atmosphere using a Ramé-Hart NRL 100 Goniometer (Ramé-Hart Inc., NJ) using the sessile and captive drop methods. At least three droplets were measured and averaged on each substrate surface to represent the correct contact angles within ±2°.

Infrared spectroscopy: The infrared reflection−absorption spectroscopy (IRAS) experiments were performed with a Bruker IFS 113v FT-IR spectrometer attached to an in-house customized UHV system equipped with a manual sample scanning and manipulation system. The infrared beam was aligned at 85° angle of incidence with respect to the surface normal and focused onto a ∼5 mm spot on the sample surface using *f*/16 optics.[25] A narrow-band MCT detector was used to detect the light, and 1000−2000 consecutive scans were averaged at 2 cm^{-1} resolution before Fourier transformation. The IRAS experiments at elevated substrate temperatures were performed in the same UHV system. The substrate surface was mounted on a copper block which could be resistively heated to 250 °C. The temperature was measured with a Pt 100 element in the copper block.

Spectral simulation: Simulated IRAS spectra of the two molecules on gold were generated form the optical constants $n(\nu)$ and $k(\nu)$ derived from the transmission−absorption (KBr) spectra of the pure compounds. The procedure has been described in detail before by several groups,[26,27] and only a brief description will be given here. The $n(\nu)$ and $k(\nu)$ set is obtained by using an iterative Kramers−Kronig algorithm. The in-put $k(\nu)$ used in that algorithm is determined from the Lambert−Beer law ($A(\nu)^{KBr} = 4\pi k(\nu)\nu d_{eff}$, where $A(\nu)^{KBr}$ is the absorbance spectrum and d_{eff} the effective thickness of the compound in the KBr pellet). The procedure is iterated by refining $n(\nu)$ (eq 1) and $k(\nu)$ until $|A(\nu_i)^{KBr} - A(\nu_i)^{calc}| < \epsilon$ (where ϵ is typically

$$n(\nu_i) = n(\infty) + \frac{2}{\pi}\int \frac{k(\nu)\nu}{\nu^2 - \nu_i^2}\delta\nu \qquad (1)$$

set to 10^{-4}). The real part of the refractive index at high frequencies $n(\infty)$ (eq 1) is taken from optical data of poly(oligo)-thiophenes and polymethylenes at visible frequencies.

The final set of $n(\nu)$ and $k(\nu)$ is the inserted in a simulation program, using a three-phase parallel slab optical model consisting of air/organic film/metal, to yield the calculated IRAS spectrum characteristic of an isotropic film of the pure compound on the substrate surface.

X-ray photoelectron spectroscopy: The XPS measurements were performed on a Scienta ESCA-300 spectrometer using monochromatized Al Kα radiation (1486.6 eV), a 30 cm (radius) analyzer, and a multichannel detection system.[28] The spectral resolution, as determined from the shape of the Fermi edge of silver, using a 0.8 mm slit and 300 eV pass energy, was approximately 0.5 eV. The photoelectrons were analyzed at two takeoff angles (TOA) 10° and 90° with respect to the plane of the surface in order to reveal the depth distribution of the atomic elements within the monolayer. The final XPS spectra presented below are obtained by averaging several spectra from different spots (typically four) on the sample surface. This procedure was used to reduce the exposure time to X-ray radiation, and thereby minimizing the risk for damaging the monolayer. Recent investigations have shown that alkanethiolate SAMs, especially the thiolate bonds, are very sensitive to prolonged exposure of X-ray radiation. [29]

Electrochemical measurements: The electrochemical cell consists of a Teflon body machined to accept a Viton O-ring in a cylindrical cavity surrounding a hole on the side of the Teflon block. The gold substrate was pressed against the Viton O-ring to reproducibly define the active area of 0.2 cm^2 exposed to the electrolyte as the working electrode. An Ag/AgCl (3 M NaCl, BAS) electrode and a platinum wire were used as reference and counter electrodes, respectively. The electrochemical measurements were performed using an Autolab electrochemical system (Eco chemie, The Netherlands). All voltammograms were recorded with a scan rate of 100 mV/s.

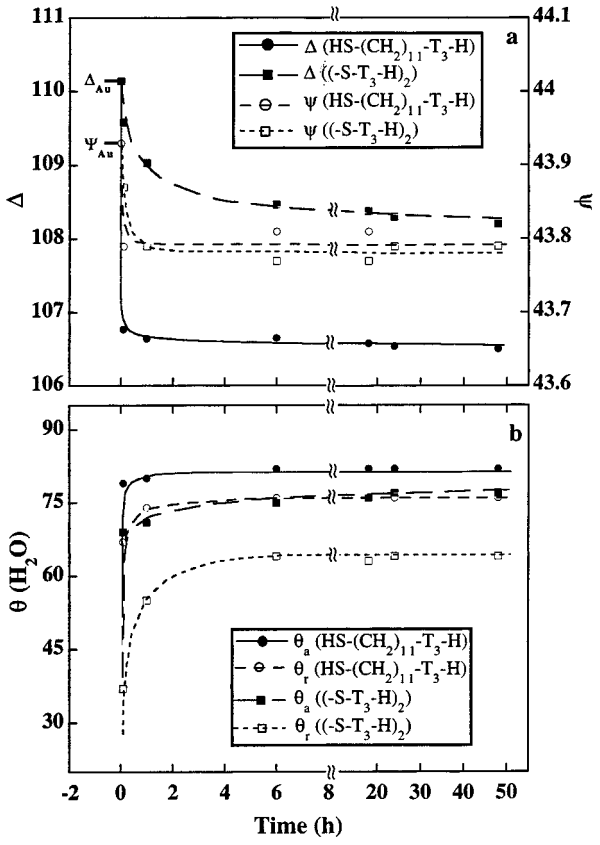

Figure 1. Formation of monolayers of $(-S-T_3-H)_2$ and $HS-(CH_2)_{11}-T_3-H$ on gold versus time: (a) Ellipsometric readings Δ and Ψ. Also included in (a) is the starting values of clean gold $(\Delta,\Psi)_{Au}$ = (110.20,43.93). (b) Advancing and receding contact angles with water. The solid and dotted line are guidelines for the eye.

Results and Discussion

Monolayer Formation. To gain insight in the kinetics and the mechanisms of monolayer formation of $(HS-(CH_2)_{11}-T_3-H)$ and $(-S-T_3-H)_2$ on gold, a series of ellipsometric and contact angle measurements were performed as function of adsorption time. The substrates were removed from the solution after 5 min, 1 h, and so on up to 48 h, (Figure 1), rinsed in EtOH, blown dry in N_2 gas, quickly analyzed with ellipsometry and contact angle measurements, and then immediately reimmersed in the sample solution.

Ellipsometry: Figure 1a shows the variation in the ellipsometric readings Δ and Ψ as function of adsorption time, starting at Δ = 110.20 and Ψ = 43.93, the values for pure "clean" gold. The Ψ values for both samples are almost identical and display only a small change with respect to the corresponding value for pure gold. Thus, the Ψ values appear to be less useful for studying the kinetics of monolayer formation. A different behavior is observed for the Δ values. The Δ values for $HS-(CH_2)_{11}-T_3-H$ decrease abruptly and levels out about 4.7° below the Δ value of pure gold. About 95% of the total change in delta Δ occurs within 5 min, indicating a rapid assembly process and that only minor in-plane reorganization (reorientation) phenomena occur within the monolayer with prolonged

TABLE 1: Experimental and Calculated Mode Frequencies ν_i and Assignments of HS−$(CH_2)_{11}$−T_3−H and (−S−T_3−H)$_2$ on Gold and Transition Moment Directions M_i (in Molecular Coordinates *L, M, N*) and Relative Peak Intensities I_i^{exp}/I_i^{calc}

HS−$(CH_2)_{11}$−T_3−H/Au				(−S−T_3−H)$_2$/Au				
ν_i^{exp} (cm^{-1})	ν_i^{calc} (cm^{-1})	$\bar{M}_i$[a]	I_i^{exp}/I_i^{calc} [b]	ν_i^{exp} (cm^{-1})	ν_i^{calc} (cm^{-1})	$\bar{M}_i$[a]	I_i^{exp}/I_i^{calc} [b]	assignments[c]
					3110	*L*		ν_0 C_β−H str.
	3095	*L*			3099	*L*		ν_0 C_β−H str.
				3083	3077	*M*	3.3	ν_0 C_β−H str.
3066	3070	*L*	3.27	3070	3065	*L*	7.1	ν_0' C_β−H str.
					3038	*M*		ν_0'' C_α−H str.
2919	2923							$\nu_{as}(CH_2)$, d$^-$ (alkyl)
2849	2845							$\nu_s(CH_2)$, d$^+$ (alkyl)
1541	1540	*L*		1523	1524	*L*		ν_1 C_α=C_β−H asym str
1511	1510	*L*	2.08	1493	1493	*L*	7.3	ν_1 C_α=C_β−H asym str
1464	1467							δ_{sc} (CH_2) (alkyl)
1454	1453	*M*	0.13	1451	1454	*M*	2.0	ν_2 C_α=C_β−H sym str
	1426	*M*	0.15[e]	1422	1427	*M*		ν_2 C_α=C_β−H sym str
				1414	1417	*M*	1.5	ν_2 C_α=C_β−H sym str
1367	1370	*L*	5.1	1365	1364	*L*	5.0	ν_3 C_β=C_β str
1335	1333				1331			
1296	1293							
1269	1268			1266				
1231	1228	*L*	2.35	1206	1219	*L*		ν_4 C_β−H bend
1199	1198	*L*	2.2	1198	1194	*L*		ν_5 C_α−C_α str
1074	1063	*L*	3.9	1078	1074	*L*	8.3	ν_6 C_α−H + C_β−H bend
					1060			
	1047	*M*		1049	1047	*M*	3.6	ν_7 C_β−H bend
					975			ν_8 C−S def + C_α−H bend
	896				896			ω_1 C−H
865	865			861	865			ν_8 C−S def + C_α−H bend
	832	*d*		836	835	*d*		ω_2 C_α−H
	790	*N*	0.058[e]	793	801	*N*	0.44	ω_3 C_β−H

[a] Transition dipole moment directions $\bar{M}_i = \partial\bar{\mu}/\partial Q_i/|\partial\bar{\mu}/\partial Q_i|$ in molecular coordinates *L, M, N* (see Figure 4). $\bar{\mu}$ is the dipole moment, and Q_i the vibrational coordinate of mode *i*. [b] I_i^{exp}, I_i^{calc} are the peak intersities in the IRAS spectra used in the orientation analysis. [c] ν_0−ν_8 are the in-plane mode numbering used by Louarn et al.[33] ν_{as}, ν_s, δ_{sc} are the asym str, sym str, and scissoring def, respectively, of the methylene groups of the alkyl chain; ω_1−ω_3 are the C−H out-of-plane modes of the thiophene rings. [d] Contradictory assignments of the transition dipole moments M_i for this mode are given in the literature (ref 15 and references therein). This mode is therefore not used in the orientation analysis. [e] When peaks disappear completely in the experimental IRAS spectra I_i^{exp} is automatically set to the noise level unless otherwise stated in the text.

adsorption time. The overall process of (−S−T_3−H)$_2$ monolayer formation is much slower than for HS−$(CH_2)_{11}$−T_3−H. For example, an adsorption time 20 h is required before reaching about 90% of the total change in $\Delta \approx 2°$, suggesting that the (−S−T_3−H)$_2$ monolayer undergoes a continuos change in thickness(density) due to various reorganization phenomena and/or exchange with molecules in the surrounding solution.

Contact angle measurements: The contact angle measurements with water are shown in Figure 1b. The advancing contact angle Θ_a for HS−$(CH_2)_{11}$−T_3−H follows a similar trend as observed with ellipsommetry, i.e., Θ_a changes abruptly from <5° (the Θ_a value for pure gold) to >95% of its steady-state value within 5 min. The advancing contact angles for (−S−T_3−H)$_2$ display a much slower kinetics. The Θ_a values increase monotonically and approach the final value 77° after about 20 h immersion time. Also reported in Figure 1b are the receding contact angles Θ_r for both compounds. The Θ_a and Θ_r values together can provide important information about the chemical and/or morphological homogeneity of the monolayer. For example, a crystalline-like all-trans assembly of *n*-alkanethiols on gold exhibit a lower hysteresis $\Delta\Theta = \Theta_a - \Theta_r$ as compared to a disordered "*gauche-rich*" assembly. The observed hysteresis of the HS−$(CH_2)_{11}$−T_3−H and (−S−T_3−H)$_2$ monolayers are almost constant, 6° and 12°, for immersion times >5 min and >1 h, respectively. For shorter exposure times the hysteresis increases to 12° (5 min) for HS−$(CH_2)_{11}$−T_3−H, and to 17° (1 h) and 31° (5 min), respectively, for (−S−T_3−H)$_2$. Adopting the above way of interpreting the contact angle hysteresis it seems reasonable to assume that the HS−$(CH_2)_{11}$−T_3−H assembly possesses a more well-defined crystalline structure than the (−S−T_3−H)$_2$ assembly. In fact, the hysteresis for HS−$(CH_2)_{11}$−T_3−H is identical with the values obtained for long-chain alkanethiols on gold.[18] One possible explanation to the difference in hysteresis may be that the two molecules exhibit different orientations and packing geometries. It is from a geometric point of view not unlikely that the bulky α-T_3 moiety near the disulfide may interfere sterically to a larger extent in forming a close-packed structure than a α-T_3 moiety far away from the pinning site, as in HS−$(CH_2)_{11}$−T_3−H. Thus, steric constraints may in this particular case influence the kinetics of monolayer formation as well as the ultimate overlayer structure of (−S−T_3−H)$_2$ SAM.

The observation that the kinetics of SAM formation of the disulfide is slower than for the thiol analogue is consistent with the observations of Tour et al.[23a] who also found that about 1 day was necessary to reach a complete monolayer of structurally related rigid-rod compounds on gold.

Infrared Spectroscopy. *Assignments:* The vibrational spectra (infrared and Raman) of α-coupled poly- and oligothiophenes have been studied in detail during recent years and are nowadays fairly well understood.[15,30−33] Louran et al.[33] presented recently a vibrational study of a series of α-oligothiophenes and found a good correlation between experimental and calculated frequencies. Table 1 summarizes the vibrational frequencies for the experimental and calculated IRAS spectra (Figures 2 and 3), together with the assignments which are based on the α-T_3 unit (C_{2v}).[33] The frequencies in our calculated IRAS spectrum of (−S−T_3−H)$_2$ (Figure 2) agree very well with the corresponding ones of the α-T_3 unit indicating a minor perturbation of the π-conjugated ring system due to −S−S− substitution at the α-position of the first ring. The change of the substituent into a −$(CH_2)_{11}$−SH tail appears to have a larger effect on the vibrational spectrum (Figure 3). For example, the two ν_1 modes (asym C_α=C_β-H str) at 1493 and 1524 cm^{-1}, respectively, for (−S−T_3−H)$_2$ are both shifted upward about 20 cm^{-1} to 1510 and 1541 cm^{-1}, respectively, for HS−$(CH_2)_{11}$−T_3−H. The ring

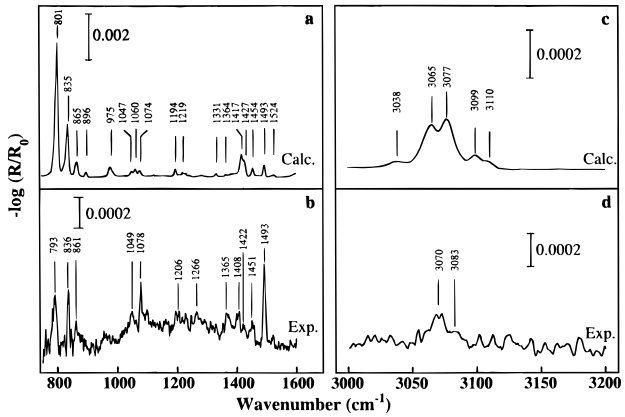

Figure 2. Calculated (a, c) and experimental (b, d) IRAS spectra of $(-S-T_3-H)_2$ on gold in the low- and high-frequency regions, respectively. The calculated spectra are obtained for a 15 Å thick film of $(-S-T_3-H)_2$ using $n_\infty = 1.7$.

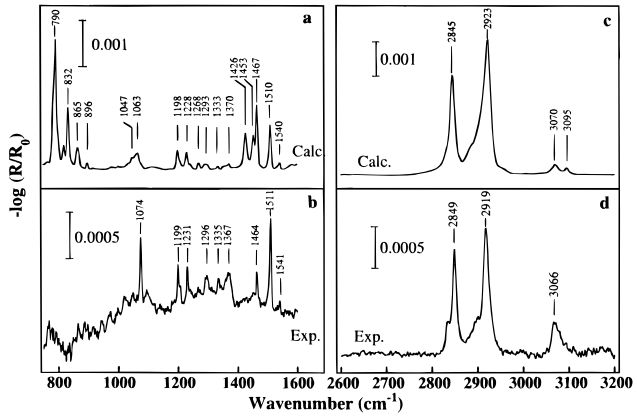

Figure 3. Calculated (a, c) and experimental (b, d) IRAS spectra of $HS-(CH_2)_{11}-T_3-H$ on gold in the low- and high-frequency regions, respectively. The calculated spectra are obtained for a 30 Å thick film of $HS-(CH_2)_{11}-T_3-H$ using $n_\infty = 1.7$.

═C−H stretching region, 3000−3100 cm^{-1}, is also different displaying five well-resolved peaks for $(-S-T_3-H)_2$ as compared to two peaks for $HS-(CH_2)_{11}-T_3-H$. We are not sure whether these changes in the calculated IRAS spectra of the compounds are entirely due to a substituent effect, or if they in part reflect a distinctly different geometrical conformation of the two compounds in the crystalline state. A different arrangement of the α-T_3 rings in the crystalline state is not unlikely for the two molecules because of their structural dissimilarities. Infrared analyses in the liquid state, performed by dissolving them in dioxane (≈1 mM) reveal, however, that the strongest ring mode (ν_1) appearing at 1493 ($(-S-T_3-H)_2$) and 1510 ($HS-(CH_2)_{11}-T_3-H$) cm^{-1} in the solid state remain unaffected upon dissolution. We find it therefore reasonable to assume that the observed differences in the calculated IRAS spectra (Figures 2 and 3) primarily are due to a substituent effect.

Experimental IRAS spectra: The experimental IRAS spectra vary substantially from the calculated ones. Although most of the peaks in the experimental spectra can be found in the calculated spectra, some of them display a very interesting behavior, in terms of frequency, line shape, and relative intensity. We start discussing the $HS-(CH_2)_{11}-T_3-H$ and the methylene stretching vibrations (Figure 3c,d) since these modes can provide valuable information about the alkyl chain conformation. Snyder et al.[34−36] have in detail investigated the methylene stretching region of polymethylenes in both the crystalline and the liquid state. They found that crystalline all-trans polymethylenes exhibited $d^-(\nu_{as}(CH_2))$ and $d^+(\nu_s(CH_2))$ modes at 2915 and 2846 cm^{-1}, respectively. In the conformationally disordered (liquid) state the d^- and d^+ modes appear at 2928 and 2856 cm^{-1}, respectively. Thus, the exact frequencies of the d^- and d^+ modes can be used as a measure of the population of gauche conformers along the polymethylene chain. The line shape (half-width) of the d^- and d^+ modes is also sensitive to the conformational status of the polymethylene chains. Half widths of 10−13 and 7−10 cm^{-1} for the d^- and d^+ modes, respectively, are generally considered to be characteristic for all-trans polymethylenes, whereas broader peaks are attributed to disordered gauche-rich chains. The above protocol has been extensively utilized to characterize the alkyl chain conformation of *n*-alkanethiols $HS-(CH_2)_m-CH_3$ SAMs on gold,[19,37−38] and the very best SAMs ($m \geq 15$) display d^- and d^+ frequencies at 2918 and 2850 cm^{-1}, respectively, i.e., close to the limiting values obtained for crystalline all-trans polymethylenes. The all-trans character is however critically dependent on the chain length, and for chain lengths $m < 12$, the chains possess an increasing population of disordered methylenes characterized by d^- and d^+ frequencies ≥2920 and ≥2851 cm^{-1}, respectively.[19] The experimental spectrum (Figure 3d) displays d^- and d^+ frequencies between 2918.7 ± 0.3 and 2849.3 ± 0.1 cm^{-1}, respectively, and half-widths of 13 and 10 cm^{-1}, respectively. To the authors knowledge, such low d^-, d^+ frequencies have not been reported before for *n*-alkanethiols with eleven methylene groups on gold, indicating an almost perfect all-trans conformation. One possible explanation to the observed results is that the α-T_3 units are organized in such a way that they are contributing substantially to the overall in-plane stabilization of the $HS-(CH_2)_{11}-T_3-H$ assembly. This is not an unlikely scenario since the geometrical arrangement in the crystalline state primarily is driven by relatively strong $\pi-\pi$ interactions between adjacent terthiophene units.

Another interesting observation in the methylene stretching region is that two new peaks appear at 2897 and 2834 cm^{-1} on the low-frequency sides of the d^- and d^+ modes. Note that the 2897 cm^{-1} peak appear at a different position as compared to the shoulder near 2880 cm^{-1} in the calculated spectrum (Figure 3c,d). A highly organized all-trans assembly is not expected to display such peaks. However, extra methylene stretching peaks have been observed before in IRAS spectra of highly organized assemblies of ω-substituted alkanethiols. For example, SAMs of $HS-(CH_2)_{16}-OH$ on gold exhibit a peak near 2878 cm^{-1}, which has been attributed to a nearest-neighbor-induced perturbation of the conformation of the outermost CH_2 group, in this case caused by the terminal hydroxyl group.[39a] We believe that this perturbation originates from the strong in-plane interaction between neighboring hydroxyl groups (hydrogen bonding). Supporting evidence for the above hypothesis was obtained in a recent study of water nucleation on hydroxyl-terminated SAMs, where we found that the 2878 cm^{-1} peak disappeared upon disturbing the lateral hydrogen-bonding pattern with a secondary adsorbate (a monolayer of water molecules).[39b] A conformationally different methylene group (rotated or twisted with respect to the all-trans backbone) may in the case of $HS-(CH_2)_{11}-T_3-H$ originate from the incomensurability between the organization and orientation of the all-trans alkyl chains and the in-plane correlations of the laterally interacting α-T_3 moieties. Thus, we believe that the two extra peaks in the methylene stretching region are due to unique methylenes near the α-T_3 terminus, in analogy with what previously have been observed for hydroxyl terminated thiols.[39a,b] Curve-fitting and integration of the 2897 and 2834 cm^{-1} peaks reveal that approximately 15% of the overall methylene intensity originates from these conformationally perturbed methylenes, suggesting perhaps that even more than one methylene group is affected by the organization of the α-T_3 moieties.

The IR results obtained so far indicate that HS−$(CH_2)_{11}$−T_3−H assembles in a highly organized state on gold, where the main part of alkyl chains appear to approach the limiting case of all-trans polymethylenes. A small part of the alkyl chain, the outermost methylene group(s), appears to undergo a conformational change which most likely is driven by lateral interactions between the α-T_3 moieties. The most striking evidence for the formation of an organized assembly can be obtained by considering the relative intensity variations between the peaks in the calculated and experimental spectra. Some of the peaks appear with enhanced intensity in the experimental spectrum, whereas others hardly can be seen at all. The most pronounced effect is observed for the 790 cm^{-1} peak, which cannot be seen in the experimental spectrum although it is by far the strongest peak in the calculated (isotropic) spectrum (Figure 3a,b). This phenomenon is due to the well-known *surface dipole selection rule*, which only allows modes with vibrational transition dipole moments aligned perpendicular to the metal substrate to interact with the IR beam and appear in the IRAS spectrum, whereas those aligned parallel with the substrate cannot be observed at all. Thus, the transition moment of the 790 cm^{-1} peak must according to this simple way of reasoning be aligned parallel to the metal substrate. A more rigorous analysis requires detailed assignments of the vibrational modes in terms of symmetry classes and transition dipole moment directions. In the following section we describe a thorough orientation analysis of the α-T_3 moiety with respect to the metal substrate for both compounds.

Orientation analysis: As mentioned above, the vibrational mode must have a component of its transition dipole moment aligned perpendicular to the metal surface in order to be infrared active. Furthermore, the intensity I_i (absorbance value) of a vibrational mode is proportional to the square of the scalar product of the electric field $\bar{E}$ and the normalized transition dipole moment $\bar{m}_i$ (the direction of the transition moment in surface coordinates), and can be written as

$$I_i = C|\bar{E}\cdot\overline{m_i}|^2 \tag{2}$$

Including the anisotropic behavior of the electric field at the surface $\bar{E} = |\bar{E}|\cdot\hat{z}$ in eq 2, where $\hat{z}$ is perpendicular to the plane of the metal and $C' = |\bar{E}|^2\cdot C$, then eq 2 can be rewritten as

$$I_i = C'|\hat{z}\cdot\overline{m_i}|^2 = C' m_{iz}{}^2 \tag{3}$$

If the film is anisotropic but otherwise identical with the reference material (e.g., in KBr), then the following expression is valid for the experimental and calculated intensities (peak heights in the IRAS spectra)

$$I_i^{\text{exp}}/3I_i^{\text{calc}} = m_{iz}{}^2 \tag{4}$$

where $3I_i^{\text{calc}}$ represents the maximum obtainable intensity in the experimental spectrum if one assumes that all m_i's are aligned parallel to the electric field ($\hat{z}$). Equation 4 requires also that the m_i's are known with respect to the molecular coordinate system ($\bar{M}_i$). The M_i's for the α-T_3 unit (*L*, *M*, *N*) (Figure 4) are taken from the available literature on α-T_n oligithiophenes.[30,33] Thus, if the M_i's are known in molecular coordinates, then one can determine their transformations (projections) m_{iz} on the $\hat{z}$-axis (the surface coordinate system) from simple model (Figure 4). Table 2 defines the trigonometric relations for m_{iz} for the *L*, *M*, and *N*-polarized modes using the α (tilt) and β (rotation) angles in Figure 4. The orientation analysis is, as a first-order approximation, based on the assumption that all three rings are coplanar. This assumption seems reasonable since only a small twisting angle (3−12°) has been observed in the crystalline state of H−T_3−H using X-ray diffraction.[40a,b] The α and β angles determined below will be only marginally affected by such a small twisting angle.

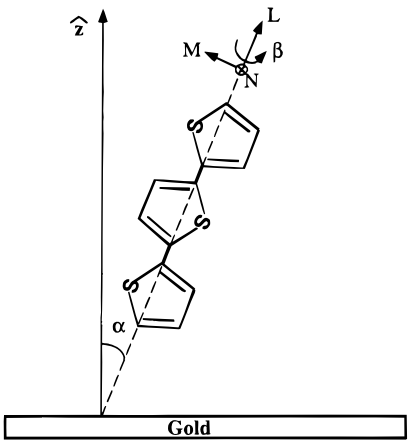

Figure 4. Model showing the tilt α and rotation β angles used in the calculation of the orientation of the terthiophene unit on gold. (*L*, *M*, *N*) defines the transition dipole moment directions of the α-T_3 unit in molecular coordinates (Table 1).

TABLE 2: Projection of the Molecular Transition Dipole Moments M_i (*L*, *M*, *N*) on the *z*-Axis, m_{iz} (the Surface Coordinate System)

M_i	m_{iz}[a]
L	cos α
M	sin α cos β
N	sin α sin β

[a] The α and β are the tilt and rotation angles defined in Figure 4.

Equation 4 can now be directly utilized to determine the α and β angles, provided that the thickness of the film is accurately determined from an independent method, e.g., ellipsometry. As mentioned before, we have not been able to fit our ellipsometric data to an optical model. We therefore have to employ a slightly different approach where mode intensities from two modes *i*, *j* are rationed to cancel the thickness dependence.[27b] Thus, by forming the ratio $A_{i,j}$ (eq 5) we can determine the angles α and β from a simple set of trigonometric equations (Table 2).

$$A_{i,j} = \frac{I_i^{\text{exp}}/I_i^{\text{calc}}}{I_j^{\text{exp}}/I_j^{\text{calc}}} = \frac{m_{iz}(\alpha,\beta)^2}{m_{jz}(\alpha,\beta)^2} \tag{5}$$

The complete orientation analysis presented here involves 9 and 11 peaks in the spectra of (−S−T_3−H)$_2$ and HS−$(CH_2)_{11}$−T_3−H, respectively. A few peaks have been omitted in the analysis because contradictory assignments are given in the literature, or if they appear on a too noisy background. Table 1 summarizes the $\bar{M}_i$'s and the relative intensities $I_i^{\text{exp}}/I_i^{\text{calc}}$ for the modes used in the analysis. Note that the factor 3 in eq 4 is omitted in Table 1 since it cancels in the final expression of $A_{i,j}$ (eq 5). The α and β angles for the HS−$(CH_2)_{11}$−T_3−H SAM are determined to equal 14 ± 4° and 33 ± 2°, respectively. Thus, the molecular axis (*L*-axis) of the α-T_3 moiety seems to be aligned nearly perpendicular to the substrate.

The reliability of the method is of course dependent on the experimental model and how accurate one can determine the peak intensities. A problem occurs when a peak disappears completely in the experimental spectrum due to a preferential alignment of its $\bar{M}_i$, cf. the 790 cm^{-1} peak in Figure 3b. How to determine its intensity? For simplicity, we have set the intensity of the disappearing peak at 790 cm^{-1} to equal the noise level in the 800 cm^{-1} region. However, since the noise level varies over the spectral range one can, as in this particular

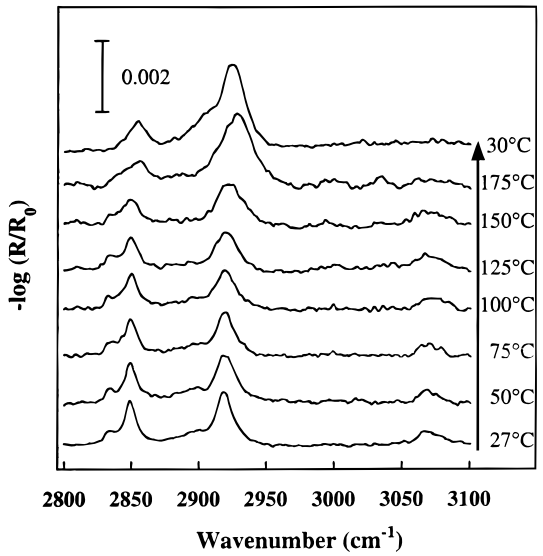

Figure 5. Evolution of the C−H stretching peaks for HS−$(CH_2)_{11}$−T_3−H on gold in the 2800−3100 cm^{-1} region as a function of substrate temperature (27−175 °C).

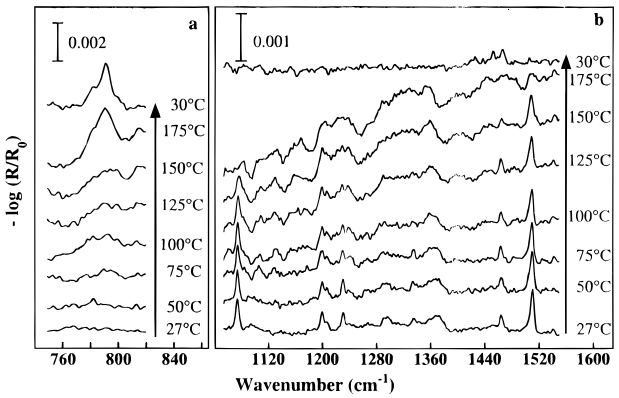

Figure 6. Evolution of the low-frequency peaks of HS−$(CH_2)_{11}$−T_3−H on gold as a function of substrate temperature (27−175 °C): (a) 750−820 cm^{-1} and (b) 1050−1550 cm^{-1}. The baseline drift appearing for temperatures ≥100 ° C is caused by thermal expansion of the sample holder.

example, easily overestimate the peak height of the disappearing feature. Thus, to investigate the sensitivity of the method, we have also calculated the α and β angles for a situation where we set the peak hight of the 790 cm^{-1} peak to half of the noise level ($I_i^{exp}/I_i^{calc} = 0.029$ in Table 1), approximately corresponding to the noise level in the high-frequency part (near 1500 cm^{-1}) of the spectrum in Figure 3b. The α and β angles obtained after such a modification are 13 ± 3.5° and 25 ± 1.5°, i.e., both angles are lower than the previous ones. The conclusion from this evaluation experiment is that the α = 14 and β = 33 should be considered as maximum values for both angles.

The tilt and rotation angles for the alkyl chain cannot be obtained using the same approach since the methylene modes in the spectra, d^-, d^+, and δ_{sc} only generate transition dipole moments in two mutually orthogonal directions (d^+ and δ_{sc} are parallel and d^- is perpendicular to the C−C−C backbone). However, if one consider a model where the all-trans (C−C−C) backbone of the alkyl chain lies in the plane defined by the $\bar{z}$-axis and the substrate, as for the α-T_3 unit (Figure 4), then we can determine the rotation angle β to equal 45 ± 2°. This β angle is in fair agreement with those previously determined for ω-substituted alkanethiols.[39a] Can we say something about the tilt angle? The absolute intensities of the d^- and d^+ modes are increased as compared to similar chain length *n*-alkanethiols suggesting that their transition dipole moments possess a more favorable orientation with respect to the surface normal. This behavior is consistent with a slightly larger tilt angle of the C−C−C backbone in the HS−$(CH_2)_{11}$−T_3−H assembly as compared to the 30° normally obtained for simple *n*-alkanethiols.

We have also determined the α and β angles for (−S−T_3−H)$_2$ assembly. The relative intensity change are less dramatic for (−S−T_3−H)$_2$ and none of the peaks disappear completely as the 790 cm^{-1} peak in the HS−$(CH_2)_{11}$−T_3−H spectrum. The angles obtained for (−S−T_3−H)$_2$ are α = 33 ± 9° and β = 23 ± 5°. Note the larger scatter in the tilt and rotation angles.

Thermal stability: We have also investigated the thermal stability of the monolayers. The evolution of the HS−$(CH_2)_{11}$−T_3−H peaks for increasing substrate temperature is shown in Figures 5 and 6. The experiments are performed in the following way: A room-temperature IRAS spectrum is taken for HS−$(CH_2)_{11}$−T_3−H; the substrate temperature is then raised to the next temperature and held at that temperature for 2 min before starting the data collection; this procedure is repeated up to 175 °C; after data collection at 175 °C, the sample is cooled to room temperature and a new spectrum is recorded. This procedure was necessary in order to be able to identify the small peaks in the 1400 cm^{-1} region, which otherwise are obscured by the baseline drift caused by thermal expansion of the sample holder (Figure 6b). Figure 5 shows the evolution of the peaks in the CH stretching region. The d^- and d^+ mode frequencies appear to remain essentially constant up to about 100 °C. Above 100 °C the peaks start to broaden and their maxima are shifted toward higher frequencies, approaching 2928 and 2857 cm^{-1} at 175 °C. This behavior indicates that complete disordering or the alkyl chains occurs at 175 °C. Although the alkyl chains appear to return to a less disordered state upon lowering the temperature back to room temperature, as revealed by the downward shift of the d^- and d^+ frequencies to 2924 and 2855 cm^{-1}, respectively (Figure 5), the overall alkyl chain conformation is still strongly disordered. The irreversible disordering temperature observed here for HS−$(CH_2)_{11}$−T_3−H, 175 °C is higher than the 125−150 °C previously obtained at our laboratory for mixed HS−$(CH_2)_{15}$−CH_3 and HS−$(CH_2)_{16}$−OH assemblies on gold. The peak intensity of the d^- mode increases substantially above 100 °C, especially between 150 and 175 °C. This increase is entirely due to a more favorable (perpendicular) orientation of the transition dipole moment of the d^- mode with respect to the surface in the disordered state.[41] The opposite trend is observed for the ring ═C−H stretching mode at 3070 cm^{-1} (*L*-polarized) which broadens with temperature and finally disappears at 175 °C. In fact all *L*-polarized modes (Table 1) behave in the same way in the temperature range 150−175 °C (Figure 6b). The only peaks remaining after the complete cycle (30 °C) in Figure 6b, are the $\delta_{sc}(CH_2)$ mode near 1467 cm^{-1} and the two *M*-polarized modes at 1453 and 1427 cm^{-1}, respectively. The ═C−H out-of-plane mode (*N*-polarized) at 790 cm^{-1}, which cannot be observed in the as-prepared spectrum (bottom spectrum of Figures 6a and 3b), displays also a remarkable increase in intensity when raising the temperature and becomes the most prominent mode in the low-frequency region.

The large upward shift of the d^- and d^+ modes accompanied by the disappearance of *L*-polarized modes and the appearance of both *M*- and *N*-polarized modes after thermal annealing at 175 °C clearly indicate a quite substantial disordering (reorientation) of the assembly, where the α-T_3 units are relaxed flat on top of a disordered "spaghetti-like" polymethylene network. Such a dramatic change in the overlayer structure cannot occur without a decrease in coverage. It is, however, not possible to exactly identify the onset of desorption from the gold surface

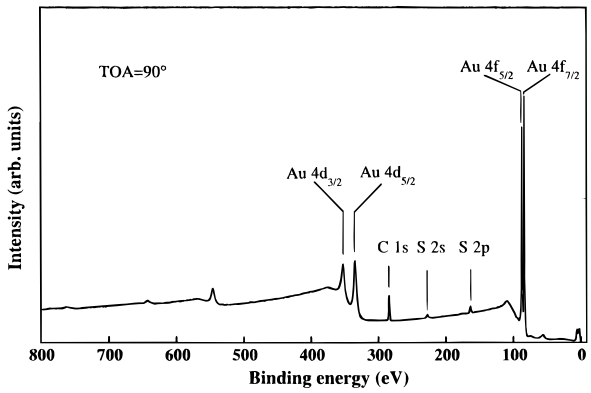

Figure 7. XPS survey spectrum of $HS-(CH_2)_{11}-T_3-H$ on gold obtained at a take of angle TOA of 90°.

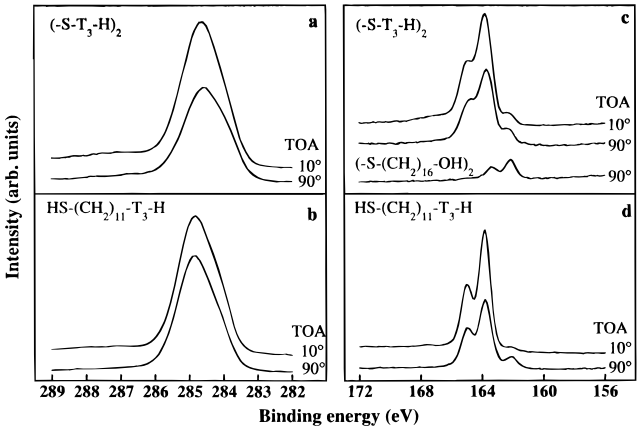

Figure 8. XPS C1s spectra for (a) $(-S-T_3-H)_2$ and (b) $HS-(CH_2)_{11}-T_3-H$ on gold obtained at two TOAs 10° and 90 °. The corresponding S2p spectra are shown in (c) for $(-S-T_3-H)_2$ and a model disulfide $(-S-(CH_2)_{16}-OH)_2$ and in (d) for $HS-(CH_2)_{11}-T_3-H$, again at two TOAs 10° and 90°.

with infrared spectroscopy, since not only the coverage but also the orientation will contribute to the infrared intensity. We can therefore only estimate that the onset of desorption most likely occurs somewhere in the interval 150−175 °C. Upon gradually increasing the temperature up to 230 °C, the rate of desorption increases, and the temperature corresponding to 50% loss of material (with respect to the coverage at 175 °C) is observed at about 205 °C. This temperature is slightly higher than for radiolabeled octadecanethiol on gold 160 °C,[42] but in fair agreement recent XPS analyses of hexadecanethiol on gold, 160−230 °C.[43] At 230 °C, the highest temperature investigated, there is still a small fraction of molecules left on the gold surface. We believe that these remaining molecules are bound more strongly to defects, steps and grain boundaries on the gold surface.

A similar set of annealing experiments were performed for $(-S-T_3-H)_2$. Due to the weak signatures in the IRAS spectra of the compound and the absence of aliphatic CH stretching modes it is more difficult to precisely identify the point of 50% loss of the molecules. Only a very week signature due to the CH out-of-plane mode at near 800 cm^{-1}, can be seen in IRAS spectra after annealing at 160 °C(not shown). We can therefore only qualitatively conclude that the $(-S-T_3-H)_2$ SAM appears to be less stable than the $HS-(CH_2)_{11}-T_3-H$ SAM.

X-ray Photoelectron Spectroscopy. *General observations:* A survey XPS spectrum of $HS-(CH_2)_{11}-T_3-H$ taken at a takeoff angle (TOA) of 90° is shown in Figure 7. The spectrum is very "clean" and displays only characteristic peaks from the gold substrate itself and from the C1s, S2s, and S2p core levels of the molecule. An almost identical survey spectrum is obtained for $(-S-T_3-H)_2$, i.e., both assemblies appear to be completely free from oxygen-containing organic as well as inorganic contaminations. The binding energies given below for the SAMs are calibrated against the $Au4f_{7/2}$ peak at 84.0 eV. The C1s peak of the $HS-(CH_2)_{11}-T_3-H$ SAM occurs at 284.77 eV (Figure 8b). The peak is asymmetric due to contributions from both thiophene (α, β) and polymethylene carbons. In a gas-phase study of bithiophene and related compounds Keane et al.[44] reported that the binding energy of the $C_\alpha-C_\alpha$ carbons were chemically shifted 0.65−0.45 eV with respect to the $C_\alpha-H$ and the C_β carbons. Therefore, the α-carbons have approximately the same binding energy as the polymethylene carbons. In the $(-S-T_3-H)_2$ spectrum the main C1s peak occurs at 284.50 eV (Figure 8a). The main feature is strongly asymmetric, with a pronounced shoulder near 283.9 eV.

Substrate interactions: A number of interesting differences can be observed when comparing the spectra of the two compounds. The main C1s peak of $(-S-T_3-H)_2$ at 284.50 eV appears at a lower binding energy as compared to the corresponding peak in $HS-(CH_2)_{11}-T_3-H$. It is also 0.3−0.4 eV lower than earlier reported C1s binding energies of α-oligothiophenes.[45−48] This peak together with a clearly visible shoulder near 283.9 eV on the low binding energy side of the main peak reveal the existence of two unique species in the $(-S-T_3-H)_2$ SAM, which to the authors knowledge have not been discussed before. To elucidate if these species are homogeneously distributed along the α-T_3 chain or if they are localized to certain parts (rings), we performed also an experiment where the C1s spectrum was collected at a TOA = 10° with respect to the surface of the sample, i.e., in a geometry where the photoelectrons from the outermost rings in the $(-S-T_3-H)_2$ assembly are expected to contribute more to the overall XPS intensity. The main C1s peak increases in intensity and shifts upward in binding energy ≈0.12 eV, and the low binding energy shoulder at 283.9 eV appears with significantly reduced relative intensity (Figure 8a), suggesting that both species originate from the $(-S-T_3-H)_2$ SAM−gold interface. Two possible explanations for their existence are proposed. Given a highly ordered $(-S-T_3-H)_2$ monolayer, it is reasonable to assume that a thiophene ring close to the disulfide (the anchoring site to gold) is more prone to change electronic structure due to charge-transfer interaction with the gold substrate than those further away, either directly via the thiophene sulfur(s) or indirectly via the thiolate sulfur at the α-position. Thus, the carbon atoms in the first, second, and third thiophene rings may not necessarily experience the same electronic environment in the ground (initial) state leading to slight shifts of their C1s binding energies. There is also another, perhaps even more important, final state contribution to binding energies originating from the image potential created by the core hole and its mirror charge in the metal, and the charge density polarization caused by these. Due to the z-dependence ($\propto 1/z$) of the image potential, it is expected to influence the kinetic energy of the photoemitted electrons originating from the interfacial region to a larger extent than those coming from the outermost part of the molecule (rings two and three). We are at present not trying to quantify the relative contributions of the initial and final state effects observed in the C1s spectrum. However, to further check the relevance of our interpretations, an identical angle-dependent experiment was performed for the $HS-(CH_2)_{11}-T_3-H$ SAM. No drastic changes are expected in this case due to the large separation between the α-T_3 unit and the metal (≈15 Å), and as can be seen in Figure 8b, the spectrum collected at 10° is virtually indistinguishable from that obtained at 90°. Thus, the two new low-energy C1s species are undoubtedly due to initial

and/or final state phenomena occurring at interfacial region between the $(-S-T_3-H)_2$ SAM and the gold substrate.

The S2p spectra of $HS-(CH_2)_{11}-T_3-H$, $(-S-T_3-H)_2$ and a model disulfide $(-S-(CH_2)_{16}-OH)_2$ are shown in Figure 8c,d. All three compounds exhibit a $S2p_{3/2}$ peak at 162.15 ± 0.1 eV. The spectrum of the $(-S-(CH_2)_{16}-OH)_2$ SAM also displays a $S2p_{1/2}$ peak (spin−orbit splitting) shifted 1.19 eV toward higher binding energies. The binding energies and relative intensities of these two peaks in the $(-S-(CH_2)_{16}-OH)_2$ spectrum are in line with the well-established picture that disulfides dissociate and chemisorb as thiolates on gold.[49,50] The thiophene S2p binding energies near 164.9 and 163.8 eV for both molecules are also in agreement with earlier reported values.[46,48] However, the S2p peaks in the $(-S-T_3-H)_2$ spectrum are slightly shifted toward lower binding energies and less well-resolved as compared to same peaks in the $HS-(CH_2)_{11}-T_3-H$ spectrum. Two obvious effects can contribute to these differences. The first one has already been discussed, and is related to the presence of nonequivalent thiophene rings in the α-T_3 unit. A superposition of XPS spectra from slightly different thiophene rings, will in the final spectrum show up as a broadening of the $S2p_{3/2}$ and $S2p_{1/2}$ peaks leading to a less well-resolved S2p signature. The S2p signature can also change because of the appearance of new species in the $(-S-T_3-H)_2$ SAM, for example, disulfides, which are expected to have peaks in the same region as the thiophene sulfur. A small fraction of disulfides can exist in the SAM because of incomplete conversion into thiolates during the chemisorption process. Recent studies of *n*-alkanethiol SAMs also have shown that Au−thiolate bonds are converted into a disulfides upon prolonged X-ray exposure.[29] This hypothesis was investigated in more detail by using the $(-S-(CH_2)_{16}-OH)_2$ SAM as a reference to monitor the X-ray-induced damages of the thiolate bond. Curve fitting and integration of the S2p peaks (disulfide and thiolate) indicate that less than 10% of the sulfurs are present as disulfides in the $(-S-(CH_2)_{16}-OH)_2$ SAM under the present experimental conditions. Although, the rate of conversion of thiolate into disulfide may vary depending on the exact nature of the tail group, we find it unlikely that such a small fraction of disulfides should have any effect whatsoever on the line shape of the much stronger thiophene S2p signature. Thus, it seems reasonable to assume that the less well-resolved S2p signature obtained for $(-S-T_3-H)_2$ is due to the presence of nonequivalent thiophene rings in the α-T_3 units (see discussion above for C1s). This latter assumption was again confirmed by collecting XPS spectra of the two samples at different takeoff angles. The $HS-(CH_2)_{11}-T_3-H$ sample displayed no shift in the two S2p peaks upon changing the TOA from 90° to 10°, indicating an identical electronic structure of the three rings. The $(-S-T_3-H)_2$ monolayer showed a more complex behavior including both a narrowing and an upward shift (≈0.10 eV) of the S2p peaks when going from a TOA of 90° to 10°. In fact, the binding energies of the S2p peaks of the $(-S-T_3-H)_2$ monolayer at 10° TOA are identical with those observed for the three identical (unperturbed) thiophene rings in the $HS-(CH_2)_{11}-T_3-H$ monolayer.

We have also used the integrated S2p (thiophene) signature at 90° TOA as a measure of the coverage (packing density) of the α-T_3 units on gold. Although the shapes of the S2p signatures are different for the two compounds, their total integrated intensities are almost the same, within 2%, suggesting that the coverage is essentially the same for the two compounds. This is an intersesting results which suggests that the ultimate packing of the two molecules is marginally dependent on the attachment of the pinning site to the α-T_3 unit (via a long alkyl tail or directly as in the disulfide). However, as has been shown by ellipsometry and contact angle measurements, the kinetics of monolayer formation is more sensitive to their structural differences.

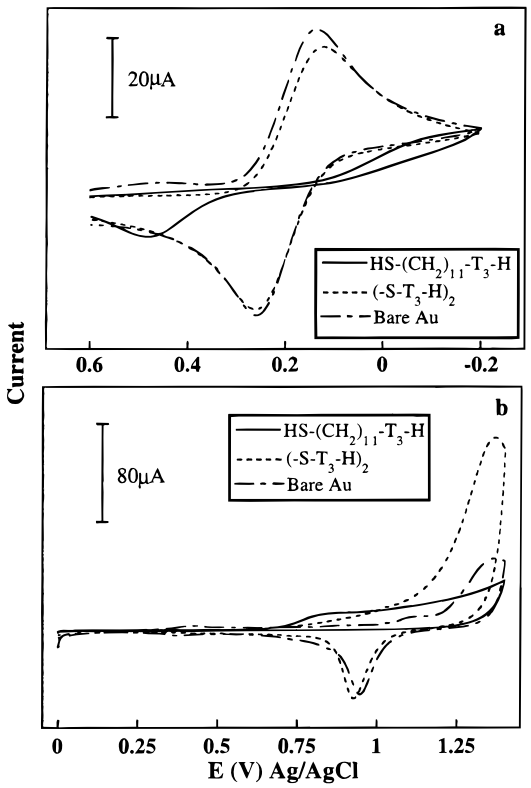

Figure 9. Cyclic voltammetric current response vs potential for $HS-(CH_2)_{11}-T_3-H$/Au, $(-S-T_3-H)_2$/Au and bare Au electrodes in (a) 1 mM $K_3Fe(CN)_6$ in 0.1 M KNO_3 solution at pH 7.0 and (b) 1 M $HClO_4$. The scan rate is 100 mV/s in both cases.

Depth distribution of the thiophene and thiolate sulfurs: Finally, we have used the integrated intensities of the thiophene and thiolate S $2p_{3/2}$ peaks obtained at different takeoff angles (TOA), 10° and 90°, to study the depth distribution of the thiolate and thiophene sulfur atoms in the SAMs. The most pronounced intensity differences are observed in the $HS-(CH_2)_{11}-T_3-H$ spectrum, where the $I_{thiophene}/I_{thiolate}$ ratio changes from 6 to 28 when altering the TOA from 90° to 10°, respectively. The corresponding intensity ratios for the $(-S-T_3-H)_2$ molecule are 5 and 10. The overall change in relative intensities by approximately a factor of 5 and 2 for $HS-(CH_2)_{11}-T_3-H$ and $(-S-T_3-H)_2$, respectively, when lowering the TOA from 90° to 10° clearly support a model where the thiophene rings are oriented toward the vacuum and the thiolates toward the metal interface. The pronounced orientation effect observed for $HS-(CH_2)_{11}-T_3-H$ is expected for a highly organized assembly of vertically oriented molecules, due to the large separation of the two sulfurs, and gives strong support to the discussion above and to the IRAS results.

Electrochemical Characterization. *Cyclic voltammetry:* The ability of a SAM to block electron transfer between the gold surface and an electrochemical probe in solution is a useful measure of the integrity of the monolayer. Compact monolayers prepared by solution self-assembly of alkanethiols on gold electrodes are generally found to inhibit diffusion of electroactive probes to the gold surface, giving a very small response in cyclic voltammetry.[51−53] The presence of defects in the monolayer increases the electrochemical response, and the appearance of the reduction/oxidation peaks in the voltammogram will depend on the exact nature of the defects. Figure 9 a shows cyclic voltammograms at gold, and at $HS-(CH_2)_{11}-T_3-H$ and $(-S-T_3-H)_2$ covered gold electrodes, respectively,

obtained in a deoxygenated 0.1 M KNO_3 solution containing 1 mM $K_3Fe(CN)_6$ at pH 7.0. The voltammogram at the $(-S-T_3-H)_2$-covered gold electrode displays almost the same electrochemical response for $Fe(CN)_6^{3-}$ as that at the bare gold electrode. The electrochemical response at the $HS-(CH_2)_{11}-T_3-H$ covered gold electrode is substantially decreased, and the potential difference between the reduction and oxidation waves of the probe is increased. Furthermore, Figure 9b shows the oxidative stripping voltammograms of the bare gold, $(-S-T_3-H)_2$- and $HS-(CH_2)_{11}-T_3-H$-covered gold electrodes in 1 M $HClO_4$. A typical pair of redox peaks appear at the bare gold electrode.[54] The $(-S-T_3-H)_2$-covered gold electrode shows again a similar behavior as for the bare gold electrode; the difference is only that a much larger oxidative current appears at high potentials. This large oxidative current is most likely composed of two parallel processes, one originating from oxidation of bare spots of gold on the electrode surface, and another from oxidation of the $(-S-T_3-H)_2$ molecule. The latter processes is accompanied by desorption of $(-S-T_3-H)_2$ from the electrode surface, as revealed by the striking similarities between the subsequent scans(not shown) and that at pure gold. The $HS-(CH_2)_{11}-T_3-H$ molecule is also oxidized on gold at potentials >0.75 V, but no reductive current can be seen in the voltammogram. This irreversible behavior of the α-T_3 unit is in line with earlier studies.[1] It should also be emphasized that the experiments are performed in aqueous solution in which the terthiophene is known to be very sensitive to attack at the α-position.

The different electrochemical responses (blocking efficiencies) observed for the covered gold electrodes clearly suggest that the two SAMs possess a distribution of different types of defects. The striking similarities between the electrochemical behavior at bare gold and $(-S-T_3-H)_2$-covered gold electrodes, both with respect to heterogeneous electron transfer to a solution species and the stripping voltammograms, suggest at first glance that a large number easily accessible bare gold spots exist on the $(-S-T_3-H)_2$-covered electrode surface. Large defects (pinholes), i.e., microelectrodes of the order of a micrometer are, however, not expected to exist for a strong soft donor−acceptor system as thiols (disulfides) on gold. Such defects would immediately become occupied (filled) by molecules in the surrounding solution during the assembly process. Nor do we believe that the $(-S-T_3-H)_2$ assembly consists of widely spaced pinholes of the order of a few nanometers (so-called ultramicroelectrodes), since the current−potential characteristics of the electron-transfer process at ultramicroelectrodes is associated with a sharp current increase at the formal potential ≈0.2 V, leading to a sigmoidal voltammetric response.[55,56] Such a voltammetric response cannot be observed. *How to explain the electrochemical behavior of the $(-S-T_3-H)_2$ assembly?* The marginally slower electron-transfer rate at the $(-S-T_3-H)_2$-covered gold electrode as compared to the rate observed at the bare gold suggests that the defects are easily accessible and widely spaced on the electrode surface. What we already know from the ellipsometric and contact angle measurements is that the $(-S-T_3-H)_2$ assembly is more heterogeneous (larger hysteresis) than the SAM prepared from $HS-(CH_2)_{11}-T_3-H$. The thickness is also smaller for $(-S-T_3-H)_2$. Moreover, the infrared analysis indicates that the tilt angle α for the α-T_3 unit as well as its scatter is larger for $(-S-T_3-H)_2$. All together, these data point in the direction of a differently organized, perhaps more open, $(-S-T_3-H)_2$ assembly which may possess a distribution of different types of defects through which the electroactive probe can diffuse and reach the gold surface. Another very interesting mechanism, which is normally not considered for highly insulating barrier layers but which must be considered for the α-oligothiophenes studied here is intra- and/or interchain electronic coupling between the electroactive solution species and the gold electrode. We are not sure whether the intrinsic conductivity of the α-T_3 unit is enough to explain the large transfer rate at the $(-S-T_3-H)_2$ electrode or if some sort of partial oxidation (doping) of the α-T_3 unit, for example caused by the electroactive probe during the potential sweep, may be required. An increase in conductivity of the conjugated system will certainly facilitate the electron transport through the assembly and lower the barrier for the electron-transfer process to the gold electrode. Note that the electron transfer in this case occurs at the $(-S-T_3-H)_2$ SAM/electrolyte interface and not at bare gold spots on the electrode surface. It is also worth mentioning that the electron-transfer process in this case can occur homogeneously over the electrode area, a favorable situation for obtaining a high electrochemical response, similar to that at the bare gold electrode. We are at present not able to separate the defect- and conductivity-mediated contributions to the overall current−potential response. However, we do believe that electronic coupling must be considered when interpreting electron transfer across conjugated barrier layers. Investigations aiming at clarifying this point are currently undertaken at our laboratories.

The $HS-(CH_2)_{11}-T_3-H$ SAM inhibits the heterogeneous electron transfer more efficiently than the $(-S-T_3-H)_2$ SAM, and no bare spots of gold (pinholes) can be detected in the stripping voltammogram indicating that the $HS-(CH_2)_{11}-T_3-H$ forms a densely packed assembly. The redox-waves in the voltammogram in Figure 9a originates most likely from another type defects so-called "shallow defects".[53] They occur at steps, kinks, grain boundaries, and other imperfections on the substrate surface where the population of molecules (chains) is expected to be more sparse than on the flat terraces. They may also occur at domain boundaries and at packing faults of the SAM. The tunneling of an electron is more likely to occur in these regions, and the exact overpotential at which the electron transfer occurs depends on the density (folding of the chains) and thickness of the SAM in this particular region. The electronic properties of α-T_3 units in the $HS-(CH_2)_{11}-T_3-H$ assembly may also influence barrier of the electron-transfer process as for $(-S-T_3-H)_2$. However, this effect is obscured by another rate-determining process governed by tunneling of electrons through sparsely populated surface regions "shallow defects".

Assessment of Monolayer Structure. The ellipsometric and wettability measurements reveal that the kinetics of monolayer formation is different for the two molecules. The kinetics of $HS-(CH_2)_{11}-T_3-H$ SAM formation is fast, and most of the changes in contact angle and thickness occur within the first 5 min of contact with the sample solution. The hysteresis is also very low and appears to be constant for adsorption times ≥5 min. These data in combination with the angle-dependent XPS and IRAS data clearly support the formation of a highly crystalline and preferentially oriented $HS-(CH_2)_{11}-T_3-H$ monolayer structure, where the alkyl chains appear to relax in an extended all-trans conformation and the $C_\alpha-C_\alpha$ axes of the α-T_3 units are tilted at an average angle of about 14° with respect to the surface normal. Thermal annealing of this monolayers also reveals that the $HS-(CH_2)_{11}-T_3-H$ assembly is, at least, equally stable as its long-chain analogues, e.g., $HS-(CH_2)_{15}-CH_3$. Stripping voltammetry furthermore suggests that it is densely packed with a low pinhole (bare gold spot) density. However, defects of a different nature do exist in the monolayer as can be seen in the voltammogram describing the heterogeneous electron transfer between electroactive probes in solution and the gold surface. These defects are referred to as "shallow defects" and appear at sparsely populated (disordered) regions

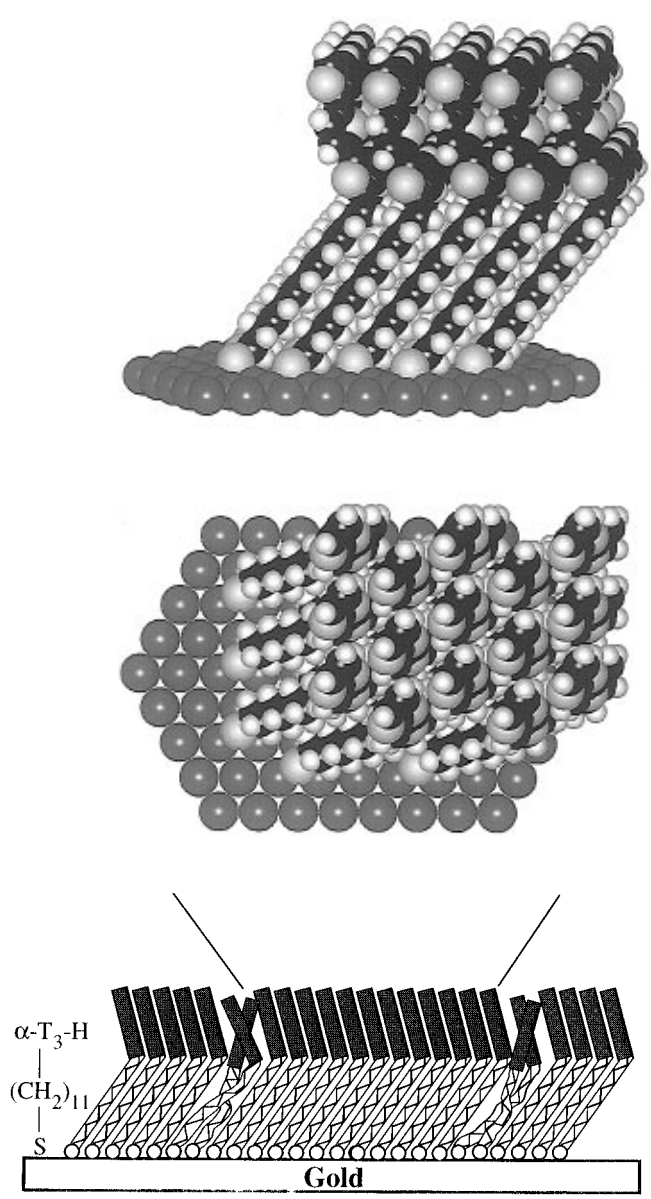

Figure 10. Proposed molecular arrangement and defect structure of $HS-(CH_2)_{11}-T_3-H$ on gold (lower panel). The tilt and rotation angles for the alkyl chains are 35° and 45°, respectively. The tilt and rotation angles (α, β) for the α-T_3 unit is −14° and 33°, respectively. See text for further details. Note that a tilt angle of −14° is inditinguishable from +14° (Figure 4). The top panel show the space-filling models of the crystalline parts of the assembly.

on the gold surface. We are currently trying to use STM to gain further insight in the distribution of the defects and the size of the crystalline domains of the $HS-(CH_2)_{11}-T_3-H$ SAM.

The structural picture emerging when summarizing all the data suggests that the $HS-(CH_2)_{11}-T_3-H$ SAM is composed of highly organized crystalline regions that are separated by shallow defects as is schematically illustrated in Figure 10 (lower panel). The crystalline parts of this model are generated from the IRAS data and recent calculations of the equilibrium structure of the $HS-(CH_2)_{11}-T_3-H$ molecule using a MINDO/3 software package.[57] The assumptions made upon generating this model are (1) the angle between the polymethylene chain axis and the $C_\alpha-C_\alpha$ axis of the α-T_3 unit is the same as in the equilibrium structure,[57] (2) the outermost methylene bonds in the all-trans chains are flexible enough to ensure a low barrier of rotation for the α-T_3 unit around its $C_\alpha-C_\alpha$ axis. The top panel, Figure 10, shows space-filling models of the top and side views of the crystalline domains of the $HS-(CH_2)_{11}-T_3-H$ SAM.

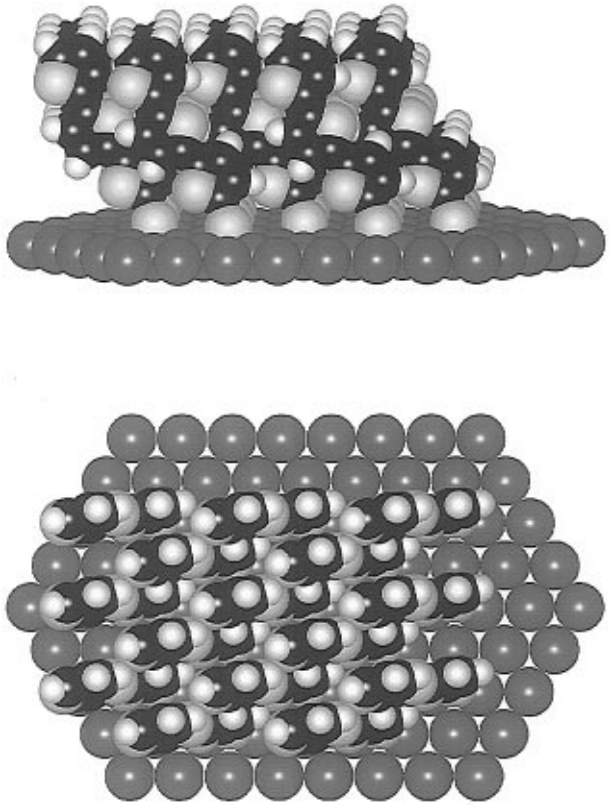

Figure 11. Space-filling models of the top and side views of $(-S-T_3-H)_2$ on gold. The tilt and rotation angles (α, β) for the α-T_3 unit is − 33° and 23°, respectively. See text for further details. Note that a tilt angle of −33° is inditinguishable from +33° (Figure 4).

The contact angle, ellipsometric, IRAS and XPS data clearly suggest that $(-S-T_3-H)_2$ also forms an organized monolayer on gold, provided that the assembly is allowed to equilibrate with the sample solution for at least 20 h. However, the tilt angle of the α-T_3 unit is larger in the $(-S-T_3-H)_2$ assembly, suggesting a more open structure, where a larger part of thiophene ring system is exposed to the ambient. A more open assembly may explain the drop in contact angles and the increase in hysteresis as compared to the more uniform $HS-(CH_2)_{11}-T_3-H$ assembly. It is, however, more difficult to present a conclusive picture of the defect structure of the $(-S-T_3-H)_2$ SAM. Figure 11 illustrates top and side views of space-filling models based on the IRAS data. Whether this assembly is open (defect rich) enough to allow for diffusion of the electroactive probe through the monolayer followed by transfer of an electron is hard to say. It should be realized, however, that these defects (if they do exist) must be widely spaced in order to explain that large electrochemical response (Figure 9a). Such a defect-rich monolayer structure is not consistent with the XPS results which postulates an almost identical coverage for the two compounds, within 2%. Thus, the alternative explanation which involves inter/intrachain (α-T_3) mediated electronic coupling between the electrochemical probe and the gold substrate is an attractive mechanism which should be explored in more detail.

Conclusions

Solution self-assembly has been used to prepare novel architectures of alkanethiol ($HS-(CH_2)_{11}-$) and disulfide ($-S-S-$) functionalized terthiophenes (α-T_3) on gold. Both molecules were found to coordinate to the gold substrate exclusively via the SH and S−S groups to yield a gold−thiolate bonds, i.e., cleavage of the S−S bond of the disulfide occurred upon chemisorption. The $HS-(CH_2)_{11}-T_3-H$ molecules assemble rapidly (minutes) leading to a highly organized and stable

overlayer structure, where the $C_\alpha-C_\alpha$ axis of the α-T_3 unit is aligned almost perpendicular to the gold surface. The formation process of the disulfide $(-S-T_3-H)_2$ assembly is much slower. Adsorption times of about 24 h are required to form a highly organized and densely packed monolayer structure. Although we are not able to give a conclusive explanation to the huge differences in the electrochemical response between the two assemblies, the results are very interesting a definitely worthy a closer examination. Of particular interest is to investigate how their electrochemical properties, e.g., defect structure, can be manipulated for the development of novel interfaces for bio- and chemical sensing.

Finally, we believe that the combination of the organosulfur surface chemistry and π-conjugated molecular materials, as the oligothiophenes, can provide a basis for the development of novel components and prototype devices for applications in the rapidly expanding field of *molecular electronics*. Investigations where self-assembled oligothiophene SAMs are used as a template for epitaxial growth of new supramolecular materials are currently undertaken.

Acknowledgment. This work was supported by the EC-HCM program ERBCHBICT941685 (B.L.) and by the Swedish Research Council for Engineering Sciences (TFR).

References and Notes

(1) Roncali, J. *Chem. Rev. (Washington, D.C.)* **1992**, *92*, 711.

(2) Bertho, D.; Jouanin, C. *Synth. Met.* **1988**, *24*, 179.

(3) Lehn, J. M. *Angew. Chem., Int. Ed. Eng.* **1988**, *27*, 89.

(4) Effenberger, F.; Schlosser, H.; Bäuerle, P.; Maier, S.; Port, H.; Wolf, H. C. *Angew. Chem., Int. Ed. Eng.* **1988**, *27*, 281.

(5) Berggren, M.; Inganäs, O.; Gustavsson, G.; Rasmusson, J.; Andersson, M. R.; Hjertberg, T.; Wennerström, O. *Nature* **1994**, *372*, 444.

(6) (a) Bäuerle, P.; Scheib, S. *Adv. Mater*. **1993**, 5, 848. (b) Bäuerle, P.; Scheib, S. *Polym. Acta* **1995**, *46*, 124.

(7) (a) Bäuerle, P.; Hiller, M.; Scheib, S.; Sokolowski, M.; Umbach, E. *Adv. Mater*. **1996**, *7*, 214. (b) Hiller, M.; Kranz, C.; Huber, J.; Bäuerle, P.; Schumann, W. *Adv. Mater*. **1996**, *7*, 219.

(8) Mehring, M. *Springer-Verlag Series in Solid State Sciences*; Springer: Berlin, 1989; Vol. 91, p 242.

(9) (a) Bäuerle, P. *Adv. Mater*. **1992**, *4*, 102. (b) Bäuerle, P.; Götz, G.; Hiller, M.; Scheib, S.; Fisher, T.; Segelbacher, U.; Bennati, M.; Grupp, A.; Mehring, M.; Stoldt, M.; Seidel, C.; Geiger, F.; Schweizer, H.; Umbach, E.; Schmeltzer, M.; Roth, S.; Engelhaaf, H. J.; Oelkrug, D.; Emele, P.; Port, H. *Synth. Met.* **1993**, *61*, 71.

(10) (a) ten Hoeve, W.; Wynberg, H.; Havinga, E. E.; Meijer, E. W. *J. Am. Chem. Soc.* **1991**, *113*, 5887. (b) Yassar, A.; Delabouglise, D.; Hmyene, M.; Nessak, B.; Horowitz, G.; Garnier, F. *Adv. Mater.* **1992**, *4*, 490. (c) Tour, J. M.; Wu, R. *Macromolecules* **1992**, *25*, 1901.

(11) (a) Geiger, F.; Stoldt, M.; Schweizer, H.; Bäuerle, P.; Umbach, E.; *Adv. Mater*. **1993**, *5*, 922. (b) Uchiyama, K.; Akimichi, H.; Hotta, S.; Noge, H.; Sakaki, H. *Synth. Met.* **1994**, *63*, 57.

(12) Horowitz, G.; Delannoy, P.; Bouchriha, H.; Deloffre, F.; Fave, J. L.; Garnier, F.; Hajlaoui, R.; Heyman, M.; Kouki, F.; Valat, P.; Wintgens, V.; Yassar, A. *Adv. Mater*. **1994**, *6*, 752.

(13) (a) Horowitz, G.; Fichou, D.; Peng, X. Z.; Xu, Z. G.; Garnier, F.; *Solid State Commun.* **1989**, *72*, 381. (b) Servet, B.; Horowitz, G.; Ries, S.; Lagorsse, O.; Alnot, P.; Yassar, A.; Deloffre, F.; Srivastava, P.; Hajlaoui, R.; Lang, P.; Garnier, F. *Chem. Mater*. **1994**, *6*, 1809. (c) Ostoja, P.; Guerri, S.; Rossini, S.; Servidori, M.; Taliani, C.; Zamboni, R. *Synth. Met.* **1993**, *54*, 447.

(14) (a) Akimichi, H.; Waragai, K.; Hotta, S.; Kano, H.; Sakaki, H. *Appl. Phys. Lett.* **1991**, *58*, 1500. (b) Waragai, K.; Akimichi, H.; Hotta, S.; Kano, H.; Sakaki, H. *Synth. Met.* **1993**, *57*, 4053.

(15) Horowitz, G.; Bachet, B.; Yassar, A.; Lang, P.; Demanze, F.; Fave, J.-L.; Garnier, F. *Chem. Mater*. **1995**, *7*, 1337.

(16) Nuzzo, R. G.; Allara, D. L. *J. Am. Chem. Soc.* **1983**, *105*, 4481.

(17) Bain. C. D.; Thoughton, E. B.; Tao, Y.-T.; Evall, J.; Whitesides; G. M.; Nuzzo, R. G. *J. Am. Chem. Soc.* **1989**, *111*, 321.

(18) Bain, C. D.; Whitesides, G. M. *J. Am. Chem. Soc.* **1989**, *111*, 7164.

(19) Atre, S. V.; Liedberg, B.; Allara, D. L. *Langmuir* **1995**, *11*, 3882.

(20) (a) Jönsson, U.; Malmqvist, M. *Adv. Biosensors* **1992**, *2*, 291. (b) Löfås, S.; Malmqvist, M.; Rönnberg, I.; Stenberg, E.; Liedberg, B.; Lundström, I. *Sensors Actuators B* **1991**, *5*, 79. (c) Liedberg, B.; Stenberg, E.; Lundström, I. *Sensors and Actuators B* **1993**, *11*, 63.

(21) (a) Champagne, G. Y.; Bélanger, D.; Fortier, G. *Bioelectrochem. Bioenergetics* **1989**, *22*, 159. (b) Albers, W. M.; Evans, P. E.; Lekkala, J.; Turner, A. P. F. *Proc. Transducers 95, Eurosensors IX*; Stockholm, Sweden, 1995; p 485.

(22) (a) Schumacher, R. *Angew. Chem., Int. Ed. Engl.* **1990**, *29*, 329. (b) Rickert, J.; Weiss, T.; Göpel, W. *Sensors Actuators B* **1996**, *31*, 45. (c) Grate, J. W.; Martin, S. J.; White, R. M. *Anal. Chem.* **1993**, *65*, 940A, 987A. (d) Bodenhöfer, K.; Hierlemann, A.; Noetzel, G.; Weimar, U.; Göpel, W. *Anal. Chem.* **1996**, *68*, 2210.

(23) (a) Tour, J. M.; Jones II, LerRoy; Pearsson, D. L.; Lamba, J. J. S.; Burgin, T. P.; Whitesides, G. M.; Allara; D. L.; Parikh; A. N.; Atre, S. A. *J. Am. Chem. Soc.* **1995**, *117*, 9529. (b) Nakamura, T.; Kondoh, H.; Matsumoto, M.; Nozoye, H. *Langmuir* **1996**, *12*, 5977. (c) Michalitsch, R.; Lang, P.; Yassar, A.; Nauer, G.; Garnier, F. *Adv. Mater.* **1997**, *9*, 321.

(24) Bertilsson, L.; Liedberg, B. *Langmuir* **1993**, *9*, 141.

(25) Engquist, I.; Lundström, I.; Liedberg, B. *J. Phys. Chem.* **1995**, *99*, 12257.

(26) Parikh, A. N; Allara, D. L. *J. Chem. Phys.* **1992**, *96*, 927.

(27) (a) Persson, N.-O.; Uvdal, K.; Liedberg, B.; Hellsten, M. *Prog. Colloid Polym. Sci.* **1992**, *88*, 100. (b) Ihs, A.; Liedberg, B. *Langmuir* **1993**, *9*, 733.

(28) Gelius, U.; Wannberg, B.; Baltzer, P.; Fellner-Feldegg, H.; Carlsson, G.; Johansson, C.-G.; Larsson, J.; Münger, P.; Vegerfors, G. J. *Electr. Spectrosc. Relat. Phenom.* **1990**, *52*, 747.

(29) Gelius, U., unpublished data.

(30) Lang, P.; Hajlaoui, R.; Garnier, F.; Desbat, B.; Buffeteau, T.; Horowitz, G.; Yassar, A. *J. Phys. Chem.* **1995**, *99*, 5492.

(31) Hotta, S.; Soga, M.; Sonoda, N. *J. Phys. Chem.* **1989**, *93*, 4994.

(32) (a) Zerbi, G.; Chierichetti, B.; Inganäs, O. *J. Chem. Phys.* **1991**, *94*, 4637. (b) Zerbi, G.; Chierichetti, B.; Inganäs, O. *J. Chem. Phys.* **1991**, *94*, 4646.

(33) Louarn, G.; Buisson, J. P.; Lefrant, S.; Fichou, D. *J. Phys. Chem.* **1995**, *99*, 11399.

(34) MacPhail, R. A.; Strauss, H. L.; Snyder, R. G.; Elliger, C. A. *J. Phys. Chem.* **1984**, *88*, 334.

(35) Snyder, R. G.; Strauss, H. L.; Elliger, C. A. *J. Chem. Phys.* **1982**, *86*, 5145.

(36) Snyder, R. G.; Marconelli, M.; Strauss, H. L.; Hallmark, V. M. *J. Chem. Phys.* **1986**, *90*, 5623.

(37) Laibinis, P. E.; Whitesides, G. M.; Allara, D. L.; Tao, Y.-T.; Parikh, A. N.; Nuzzo, R. G. *J. Am. Chem. Soc.* **1991**, *113*, 7152.

(38) Laibinis, P. E.; Nuzzo, R. G.; Whitesides,.G. M. *J. Phys. Chem*, **1992**, *96*, 5097.

(39) (a) Nuzzo, R. G.; Dubois, L. H.; Allara, D. L. *J. Am. Chem. Soc.* **1990**, *112*, 558. (b) Engquist, I.; Liedberg, B., unpublished work.

(40) (a) Hotta, S.; Waragai, K. *Adv. Mater.* **1993**, *5*, 896. (b) van Bolhius, F.; Wyhnberg, H.; Havinga, E. E.; Meijer, E. W.; Staring, E. G. J. *Synth. Met.* **1989**, *30*, 381.

(41) Parikh, A. N.; Liedberg, B.; Atre, S. V.; Ho, M.; Allara, D. L. *J. Phys. Chem.* **1995**, *99*, 9996.

(42) Schlenoff, J. B.; Li, M.; Ly, H. *J. Am. Chem. Soc.* **1995**, *117*, 12528.

(43) Nuzzo, R. G.; Fusco, F. A.; Allara, D. L. *J. Am. Chem. Soc.* **1987**, *109*, 2358.

(44) Keane, M. P.; Svensson, S.; Naves de Brito, A.; Correia, N.; Lunell, S.; Sjögren, B.; Inganäs, O.; Salaneck, W. R. *J. Chem. Phys.* **1990**, *93*, 6357.

(45) Oeter, D.; Ziegler, Ch.; Göpel, W. *Synth. Met.* **1993**, *61*, 147.

(46) Oeter, D.; Ziegler, Ch.; Göpel, W.; Naarmann, H. *Ber. Bunsen-Ges. Phys. Chem.* **1993**, *97*, 448.

(47) Oeter, D.; Ziegler, Ch.; Göpel, W.; Naarmann, H. *Synth. Met.* **1994**, *67*, 267.

(48) Dannetun, P.; Boman, M.; Stafström, S.; Salaneck, W. R.; Lazzaroni, R.; Fredriksson, C.; Brédas, J. L.; Zamboni, R.; Talini, C. *J. Chem. Phys.* **1993**, *99*, 664.

(49) Nuzzo, R. G.; Zegarski, B. R.; Dubois, L. H. *J. Am. Chem. Soc.* **1987**, *109*, 733.

(50) Biebuyck, H. A.; Whitesides, G. M. *Langmuir* **1993**, *9*, 1766.

(51) Porter, M. D.; Bright, T. B.; Allara, D. L.; Chidsey, C. E. D. *J. Am. Chem. Soc.* **1987**, *109*, 3559.

(52) Miller, C.; Cuendet, P.; Grätzel, M. *J. Phys. Chem.* **1991**, *95*, 877.

(53) Becka, A. M.; Miller, C. J. *J. Phys. Chem.* **1992**, *96*, 2657.

(54) Finklea, H. O.; Avery, S.; Lynch, M.; Furtsch, T. *Langmuir* **1987**, *3*, 409.

(55) Finklea, H. O.; Snider, D. A.; Fedyk, J.; Sabatani, E.; Gafni, Y.; Rubinstein, I. *Langmuir* **1993**, *9*, 3660.

(56) Yang, Z. P.; Engquist, I.; Kauffmann, J.-M.; Liedberg, B. *Langmuir* **1996**, *12*, 1704.

(57) Rummel, R. M. Diplomarbeit, University of Tübingen, 1994.